



# Constructing Bi<sub>2</sub>O<sub>3</sub>/BiOIO<sub>3</sub> triple heterojunction doped with Yb<sup>3+</sup> ions as accelerating charge carriers transfer channel to enhance photocatalytic activity

Tong Li <sup>a,1</sup>, Siyuan Ren <sup>a,1</sup>, Jiang Wu <sup>a,b,\*</sup>, Min Zhou <sup>c</sup>, Cheng Peng <sup>a</sup>, Hai Zhang <sup>d</sup>, Ping He <sup>a</sup>, Xuemei Qi <sup>a</sup>, Mao Song <sup>a</sup>, Yuzhuo Zhou <sup>a</sup>, Shuo Chen <sup>a</sup>

<sup>a</sup> College of Energy and Mechanical Engineering, Shanghai University of Electric Power, Shanghai, 200090, China

<sup>b</sup> Shanghai Non-carbon Energy Conversion and Utilization Institute, Shanghai, 200240, China

<sup>c</sup> The Third Thermoelectrical Plant of North United Power Limited Liability Company, BaoTou, 014040, China

<sup>d</sup> School of Mechanical Engineering, Shanghai Jiaotong University, 200240, China

## ARTICLE INFO

### Keywords:

Triple heterojunction  
Yb<sup>3+</sup> doping  
Yb<sup>3+</sup>-Bi<sub>2</sub>O<sub>3</sub>/BiOIO<sub>3</sub>  
Hg<sup>0</sup> removal

## ABSTRACT

Yb<sup>3+</sup>-Bi<sub>2</sub>O<sub>3</sub>/BiOIO<sub>3</sub> heterojunction photocatalyst was successfully prepared by EG assisted hydrothermal method and calcination method. Bi<sub>2</sub>O<sub>3</sub> has a variety of crystal structure. Doped different proportion of Yb<sup>3+</sup> will lead to lattice phase transition of Bi<sub>2</sub>O<sub>3</sub>. When the amount of Yb<sup>3+</sup> doped in the complex is 1 mol%, the two crystal phases of Bi<sub>2</sub>O<sub>3</sub> coexist. α-Bi<sub>2</sub>O<sub>3</sub>, β-Bi<sub>2</sub>O<sub>3</sub> and BiOIO<sub>3</sub> are compounded in pairs to form a triple heterostructure, which constructs a unique electron transmission channel and promotes the separation of photo-generated carriers. At the same time, Yb<sup>3+</sup> has unique electronic transition characteristics, effectively broadening the spectral response range of Yb<sup>3+</sup>-Bi<sub>2</sub>O<sub>3</sub>/BiOIO<sub>3</sub> photocatalyst, which can respond to 850–1100 nm near-infrared light. The photocatalytic activity is greatly improved. Due to its optimized performance, the best efficiency of Yb<sup>3+</sup>-Bi<sub>2</sub>O<sub>3</sub>/BiOIO<sub>3</sub> triple heterojunction photocatalyst to remove gaseous Hg<sup>0</sup> under visible light can reach 76.73%, which is much higher than its pure component. Finally, the possible mechanism of photocatalysis is proposed, which provides a new idea for the construction of high-performance photocatalysts.

## 1. Introduction

With the development of science-technology and industry, the environmental pollution and energy crisis are intensifying. Among them, mercury in coal-fired flue gas has attracted great attention due to its high toxicity, bioaccumulation and long-distance atmospheric transport [1]. Mercury in the flue gas of coal-fired power plants usually exists in three forms, namely elemental mercury (Hg<sup>0</sup>), particulate mercury (Hg<sup>P</sup>) and mercury oxide (Hg<sup>2+</sup>) [2]. Compared with Hg<sup>2+</sup> and Hg<sup>P</sup>, the external electron orbit of Hg<sup>0</sup> is 1S<sup>2</sup>2S<sup>2</sup>P<sup>6</sup>3S<sup>2</sup>P<sup>6</sup>D<sup>10</sup>4S<sup>2</sup>P<sup>6</sup>D<sup>10</sup>F<sup>14</sup>5S<sup>2</sup>P<sup>6</sup>D<sup>10</sup>6S<sup>2</sup>, which is saturated [3]. The ground state is spherically symmetric, so Hg<sup>0</sup> has low polarizability and large ionization energy, resulting in low water solubility and high volatility. This makes it difficult to directly eliminate by the traditional smoke pollution control equipment [4,5]. Among many new mercury removal technologies, photocatalytic oxidation technology can

photocatalytic oxidize Hg<sup>0</sup> to Hg<sup>2+</sup> under visible light, which not only does not cause secondary pollution to the environment, but also can be recycled. Therefore, it is widely concerned [6].

Photocatalyst is the key to affect the photocatalytic oxidation technology. The specific factors are reflected in the spectral absorption, energy band structure and the separation efficiency of photogenerated electron holes [7,8]. Among many semiconductor catalysts, bismuth-based catalysts have attracted extensive attention in recent years due to their unique electronic structure, suitable band gap and adjustable surface structure. Common bismuth-based photocatalyst materials can be divided into three categories: bismuth-based metal composite oxides, bismuth halide oxides (BiOX, X = Cl, Br, I) and bismuth oxide (Bi<sub>2</sub>O<sub>3</sub>) [9–11]. Among them, bismuth oxyiodate (BiOIO<sub>3</sub>) has low toxicity and unique crystal structure [12,13]. The special (Bi<sub>2</sub>O<sub>2</sub>)<sup>2+</sup> layer and interlayer (IO<sub>3</sub>)<sup>-</sup> anion enable it to generate internal electric field (IEF), promote the separation of photogenerated dipole

\* Corresponding author. No. 2103 Pingliang Road, Shanghai, 200090, China.

E-mail address: [wjcfd2002@163.com](mailto:wjcfd2002@163.com) (J. Wu).

<sup>1</sup> These authors contributed equally to this work.

pairs, and improve the photocatalytic performance [14–16]. However, in practical applications,  $\text{BiOIO}_3$  is usually limited by a relatively large band gap (about 3.07 eV) and a small absorption boundary (about 410 nm) [13]. The higher photogenerated carrier recombination rate leads to the opposite result. Therefore, people have explored various methods to improve the catalytic activity of  $\text{BiOIO}_3$ , such as morphology regulation, element doping and heterostructure construction [6,17–19].  $\text{Bi}_2\text{O}_3$  has a simple synthesis and low toxicity. Due to the symmetry of its cell,  $\text{Bi}_2\text{O}_3$  exists in more than one crystal form, namely monoclinic ( $\alpha$ ), tetragonal ( $\beta$ ), body-centered cubic ( $\gamma$ ), face-centered cubic ( $\delta$ ), orthogonal ( $\epsilon$ ), triclinic ( $\omega$ ) and hexagonal crystal systems [20]. Among them,  $\alpha$  and  $\delta$  phases are thermodynamically stable, while  $\beta$ ,  $\gamma$  and  $\omega$ - $\text{Bi}_2\text{O}_3$  are metastable. In this work, generally  $\text{Bi}_2\text{O}_3$  refers to  $\alpha$ - $\text{Bi}_2\text{O}_3$ . Each  $\text{Bi}_2\text{O}_3$  polymorph has a different electronic band configuration, which can selectively transform between crystalline phases through reasonable technological conditions [21]. Compared with  $\text{BiOIO}_3$ ,  $\text{Bi}_2\text{O}_3$  has a narrow band gap energy range ( $E_g = 2.6\text{--}2.9$  eV) and can be excited by partial visible light (spectral absorption boundary is about 445 nm) and ultraviolet wavelength. Due to the difference in the unique energy band and spectral response range in between, we can consider preparing heterojunction photocatalysts by combining  $\text{Bi}_2\text{O}_3$  and  $\text{BiOIO}_3$ , which can improve the separation efficiency and spectral response range of photogenerated electron-holes of the catalyst materials.

Element doping can effectively adjust the crystalline phase and morphology of the catalyst, so as to improve its energy band structure [22]. Rare earth ions doping can effectively broaden the spectral response while adjusting the band structure. On the one hand, the radius of rare earth ions is close to that of  $\text{Bi}^{3+}$  ions, and rare earth ions can easily enter  $\text{Bi}_2\text{O}_3$  by doping to replace  $\text{Bi}^{3+}$ , making its lattice phase transition [23–26]. Zhao et al. controlled the morphology and crystal phase of  $\text{Bi}_2\text{O}_3$ :  $\text{Yb}^{3+}/\text{Tm}^{3+}$  by changing the  $\text{Yb}^{3+}$  doping concentration. With the increase of  $\text{Yb}^{3+}$  doping concentration (0–40%), it can be observed that the morphology of  $\text{Bi}_2\text{O}_3$  changes from nano sheet to nano flower to nano ball, and the crystal phase also changes from monoclinic phase to tetragonal phase and finally to cubic phase [27]. Parada Siriwong et al. found that by changing the preparation conditions of the catalyst, the primary and secondary phases of the crystal can coexist and interact with each other to further promote the photocatalytic activity [28]. On the other hand, the stable valence state of rare earth ions is trivalent. From  $\text{Ce}^{3+}$  to  $\text{Yb}^{3+}$ , their electronic configuration is  $[\text{Xe}]4f^n$  ( $n = 1, 2, 3 \dots, 13$ ). Due to its unique electronic layer structure,  $n$  4f electrons that are not filled in the shell can be arranged randomly among the seven spin orbits, resulting in a variety of 4f electron energy levels of these rare earth elements. The transition of 4f electrons between these different energy levels produces absorption and emission from infrared to ultraviolet. Therefore, rare earth ion doping can effectively cause the absorption edge red shift of the photocatalyst, broadening its light response range and improving its light utilization.  $\text{Yb}^{3+}$  has a simple energy level and a wide absorption peak, which decides to doping  $\text{Yb}^{3+}$  into  $\text{Bi}_2\text{O}_3$ .

Therefore,  $\text{Yb}^{3+}\text{-}\text{Bi}_2\text{O}_3/\text{BiOIO}_3$  photocatalyst was successfully prepared by EG-assisted hydrothermal method and calcination method, and its photocatalytic activity for the oxidation of  $\text{Hg}^0$  under visible light irradiation was evaluated. In addition, combined with a series of characterization methods and theoretical calculations, the physical structure, surface morphology, electrochemical properties, optical properties and the mechanism of action with photocatalytic oxidation of  $\text{Hg}^0$  of  $\text{Yb}^{3+}\text{-}\text{Bi}_2\text{O}_3/\text{BiOIO}_3$  composite photocatalyst were investigated in detail and fully discussed.

## 2. Experimental section

### 2.1. Materials and preparation

In this work, all chemicals such as  $\text{Bi}(\text{NO}_3)_3\cdot 5\text{H}_2\text{O}$ ,  $\text{Yb}(\text{NO}_3)_3$ ,  $\text{KIO}_3$ ,

ethylene glycol, anhydrous ethanol and deionized water are analytical grade reagents without further purification. They were all purchased from Sinopharm Chemical Reagent Co., Ltd.

#### 2.1.1. Synthesis of $\text{BiOIO}_3$ and $\text{Yb}^{3+}\text{-}\text{Bi}_2\text{O}_3/\text{BiOIO}_3$

$\text{Yb}^{3+}\text{-}\text{Bi}_2\text{O}_3/\text{BiOIO}_3$  photocatalyst was prepared with hydrothermal method followed by calcination. The experimental process is as follows.

##### (1) Preparation of $\text{BiOIO}_3$ :

3 mmol  $\text{Bi}(\text{NO}_3)_3\cdot 5\text{H}_2\text{O}$  and 3 mmol  $\text{KIO}_3$  were dissolved in 50 mL deionized water and stirred by magnetic force at room temperature for 30 min to form a homogeneous mixed solution. The above solution was transferred to a stainless steel autoclave with 100 mL, hydrothermally heated at 160 °C for 12 h. After cooling to room temperature, it was washed three times with ethanol and deionized water, respectively, and dried at 80 °C overnight to obtain  $\text{BiOIO}_3$  precursor.

##### (2) Preparation of $\text{Yb}^{3+}\text{-}\text{Bi}_2\text{O}_3/\text{BiOIO}_3$ :

1 mmol  $\text{Bi}(\text{NO}_3)_3\cdot 5\text{H}_2\text{O}$ , 0.5 g urea, a certain amount of  $\text{Yb}(\text{NO}_3)_3\cdot 5\text{H}_2\text{O}$  and 1 mmol  $\text{BiOIO}_3$  were dissolved in 20 mL EG solution respectively. They were completely dissolved by ultrasonic vibration to form reaction solutions A, B, C and D. Solution C was added to solution A and stirred magnetically for 30 min. Then, solution B was added to the mixture of A and C and stirred for about 30 min, then solution D was added to the mixture of A, B and C and stirred for 1 h at room temperature. The final mixed solution was transferred to a 150 mL PTFE lined stainless steel autoclave, hydrothermally heated at 160 °C for 12 h, and then cooled naturally. The precursor was washed with water and ethanol for three times, respectively. Then the samples were put into the drying oven and dried at 80 °C for 10 h. In the end, the above-prepared samples were placed in a muffle furnace and calcined in air at 500 K for 2 h, and the heating rate was 2 °C min<sup>-1</sup>, which is a suitable calcination temperature according to our previous research [29]. The final photocatalyst sample obtained is expressed as YBB-X, where X represents the molar percentage (mol%) of  $\text{Yb}(\text{NO}_3)_3\cdot 5\text{H}_2\text{O}$  in the compound, X = 0, 1, 10. The samples were named YBB-0, YBB-1 and YBB-10, respectively.

## 2.2. Characterization

The crystal phase structure of the as-prepared catalysts was studied by X-ray powder diffraction (XRD, Bruker D8, Germany) using  $\text{Cu K}\alpha$  as the radiation source, and the range of  $2\theta = 20\text{--}70^\circ$  was scanned at a scanning rate of 2°/min. The microstructure and morphology of the samples were observed by scanning electron microscopy (SEM, Germany Leo 1530vp) and transmission electron microscopy (TEM, Model CM200). High resolution transmission electron microscopy (HRTEM) further recorded the internal arrangement and lattice fringes of the crystals. The chemical states and chemical bonds of the as prepared samples were characterized by PHI-5300 X-ray photoelectron spectroscopy (XPS), which was made in the United States, and the radiation source was  $\text{Al K}\alpha$  Line. On this basis, the adsorption/desorption curves of  $\text{N}_2$  were measured by Micromeritics ASAP 2020, and the specific surface area of the catalyst was calculated by Brunauer–Emmett–Teller (BET) method. And ultraviolet-visible diffuse reflection spectrum (UV-vis DRS, UV-3600 Plus) was used to study the light absorption characteristics of the catalyst in the range of 200–1000 nm. The photoluminescence (PL) of the samples was determined by PL (F-4600 FL spectrophotometer) with excitation wavelength of 330 nm.

### 2.3. Electrochemical measurements

The electrochemical tests were carried out on the electrochemical workstation (CHI660E) with standard three-electrode cell. Fluorine doped tin oxide (FTO) glass was used as working electrode, Pt as counter

electrode and Ag/AgCl as reference electrode. 10 mg of the as-prepared catalyst was added to 20 µg Nafion solution and 1 mL ethanol mixed solution and treated by ultrasound, then evenly coated on the conductive side of clean FTO glass. The electrochemical impedance spectroscopy (EIS) and transient photocurrent response (PC) of the samples were studied by using a 300 W xenon lamp and a 400 nm filter as the light source, and the Mott Schottky curve was measured at 1000 Hz in the dark.

#### 2.4. Photocatalytic activity tests

The photocatalytic activity of the YBB composite photocatalyst was evaluated with the efficiency of removing gas phase elemental mercury. The experimental equipment includes simulated flue gas system, photocatalytic reactor system and mercury on-line monitoring system, which we have studied before [30]. At room temperature, the total flow rate of 5% O<sub>2</sub> + N<sub>2</sub> gas in the release cylinder is 1.2 L/min, which is divided into two branches, one of which carries Hg<sup>0</sup> steam through the mercury generator system (PSA) at a speed of 0.2 L/min, and the other branch has a flow rate of 1.0 L/min. Two kinds of gas flow are accurately controlled by mass flowmeter (MFC, CS200). The temperature of the mercury steam generator is controlled at 50 °C to ensure its stable mercury concentration. When the main two-way valve is opened and the bypass two-way valve is closed, the carrier gas carries mercury vapor into the photocatalytic reaction system to react with the photocatalyst. The concentration of Hg<sup>0</sup> in the gas phase was monitored by a mercury on-line monitor (RA-915 M). During the experiment, 50 mg of catalyst was dispersed in 10 mL of ethanol and evenly dispersed in quartz glass (75 mm × 75 mm), and then put into the photocatalytic reactor for photocatalytic activity tests under visible light and near-infrared light. After the reaction, the waste gas was purified by activated carbon and a 0.1 mol/L potassium permanganate glass bottle and then entered the atmosphere.

Finally, the photocatalytic efficiency of gas phase mercury could be obtained by the following equation:

$$\eta_{Hg^0} (\%) = \left( 1 - \frac{C}{C_0} \right) * 100\% \quad (1)$$

where C<sub>0</sub> and C represented inlet and outlet gas-phase Hg<sup>0</sup> concentration (µg/m<sup>3</sup>) of photocatalytic system.

#### 2.5. Computational method

The density functional theory (DFT) calculations are carried out on the Cambridge Serial Total Energy Package (CASTEP) codes. The exchange and correlation effects were described by the Perdew-Burke-Ernzerhof (PBE) functional within generalized gradient approximation (GGA). An energy cutoff of 489.8 eV was used. The convergence criteria were as follows: maximal force on the atoms 0.05 eV/Å, maximal stress on the atoms 0.1 GPa, maximal atomic displacement 0.002 Å, and maximal energy change per atom 2.0 × 10<sup>-5</sup> eV.

### 3. Results and discussion

#### 3.1. Crystal and phase analysis

The composition and crystallinity of the samples were measured by X-ray diffraction (XRD). Fig. 1 shows the XRD spectra of pure Bi<sub>2</sub>O<sub>3</sub>, BiOIO<sub>3</sub> and final products doped with different concentrations (X = 0, 1, 10) of Yb<sup>3+</sup>. The diffraction peak of BiOIO<sub>3</sub> is consistent with that of standard card JCPDS#26–2019 [31]. Compared with the α-Bi<sub>2</sub>O<sub>3</sub> standard card (JCPDS#41–1449), the characteristic diffraction peaks 2θ of prepared Bi<sub>2</sub>O<sub>3</sub> are 25.7°, 26.9°, 27.4°, 28°, 33.2°, 43.6°, 52.9° and 55.5°, respectively. The reflection peaks corresponding to (002), (111), (120), (012), (200), (041), (231) and (222) of α-Bi<sub>2</sub>O<sub>3</sub> monoclinic crystal

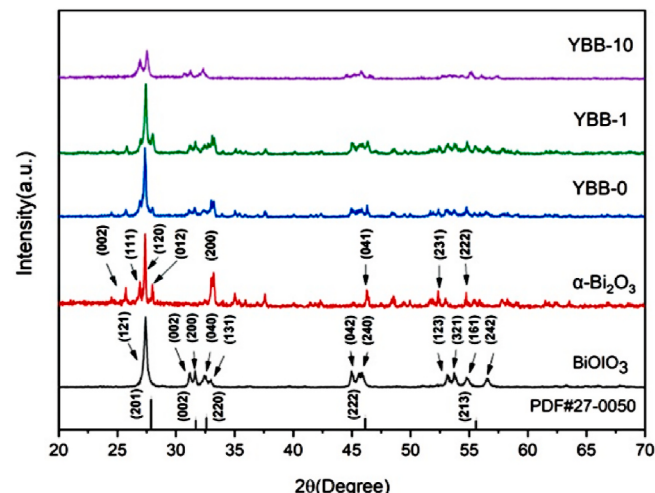


Fig. 1. XRD full spectrum of sample BiOIO<sub>3</sub>/Yb<sup>3+</sup>-Bi<sub>2</sub>O<sub>3</sub>.

indicate that the crystal form of the material is α-Bi<sub>2</sub>O<sub>3</sub>, without impurities. When Yb<sup>3+</sup> was added to the YBB mixture at 0 mol%, no additional wave peaks were observed in the image, indicating that no other crystal phase was generated. When the Yb<sup>3+</sup> doped ratio is 1 mol%, the X-ray diffraction patterns show that 2θ is equal to 27.9°. It belongs to the structural peak of tetrahedral β-Bi<sub>2</sub>O<sub>3</sub> (JCPDS 27–0050), which corresponds to the (201) plane of the material, i.e. The coexistence phase structure of α-Bi<sub>2</sub>O<sub>3</sub> and β-Bi<sub>2</sub>O<sub>3</sub> exists in the prepared composite samples. When the concentration of Yb<sup>3+</sup> increases to 10 mol%, the phase transition of Bi<sub>2</sub>O<sub>3</sub> can be clearly observed. The reason is that the radius of Bi<sup>3+</sup> is 103 p.m., which is close to the radius of rare earth ions. Rare earth ions easily enter into the Bi<sub>2</sub>O<sub>3</sub> lattice to replace some Bi<sup>3+</sup>, resulting in Bi<sub>2</sub>O<sub>3</sub> phase transition. After Yb<sup>3+</sup> doped Bi<sub>2</sub>O<sub>3</sub> is coupled with BiOIO<sub>3</sub>, there is no change in the structure peak of BiOIO<sub>3</sub> and no other impurity diffraction peak, indicating that neither Yb<sup>3+</sup> doping nor the combination with Bi<sub>2</sub>O<sub>3</sub> will lead to a new crystal orientation of BiOIO<sub>3</sub>. With the increase of the proportion of Bi<sub>2</sub>O<sub>3</sub> in the composite, the diffraction peak intensity of BiOIO<sub>3</sub> decreases gradually, which indicates that the coupling between Bi<sub>2</sub>O<sub>3</sub> and BiOIO<sub>3</sub> is successful.

#### 3.2. Morphology and structure analysis

SEM and TEM analysis were performed on the prepared samples to observe the microstructure difference of pure samples BiOIO<sub>3</sub>, Bi<sub>2</sub>O<sub>3</sub>, and YBB composite photocatalyst. SEM diagrams of BiOIO<sub>3</sub>, Bi<sub>2</sub>O<sub>3</sub>, YBB-0, YBB-1, and YBB-10 photocatalysts are shown in Fig. 2 (a)-(e). From the SEM images of the pure samples BiOIO<sub>3</sub> and Bi<sub>2</sub>O<sub>3</sub> in Fig. 2 (a) and (b), it can be seen that BiOIO<sub>3</sub> has a smooth surface and a neat edge, which is a layered structure with good crystallinity. Bi<sub>2</sub>O<sub>3</sub> particles are peanut-like and evenly distributed, and a small amount of agglomeration is caused by the calcination process. In Fig. 2 (c), Bi<sub>2</sub>O<sub>3</sub> was successfully loaded onto BiOIO<sub>3</sub>. After the introduction of 1 mol% Yb<sup>3+</sup>, the morphology of Bi<sub>2</sub>O<sub>3</sub> in Fig. 2 (d) changes. After the introduction of 10 mol% Yb<sup>3+</sup>, the morphology of Bi<sub>2</sub>O<sub>3</sub> in Fig. 2 (e) changes more obviously, the particle size increases, and the agglomeration phenomenon aggravates, which has a great relationship with the crystal transformation of Bi<sub>2</sub>O<sub>3</sub>, indicating that the doped of Yb<sup>3+</sup> can cause the crystal transformation of Bi<sub>2</sub>O<sub>3</sub>, and the crystal transformation is also different with the doping amount.

It can be clearly seen from TEM images that the transparent layered structure is in great contact with the shadowed irregular particle structure. In order to further illustrate the bonding mode between different phases of BiOIO<sub>3</sub> and Bi<sub>2</sub>O<sub>3</sub>, a high-resolution projection electron microscope (HRTEM) was placed on the contact surface of the

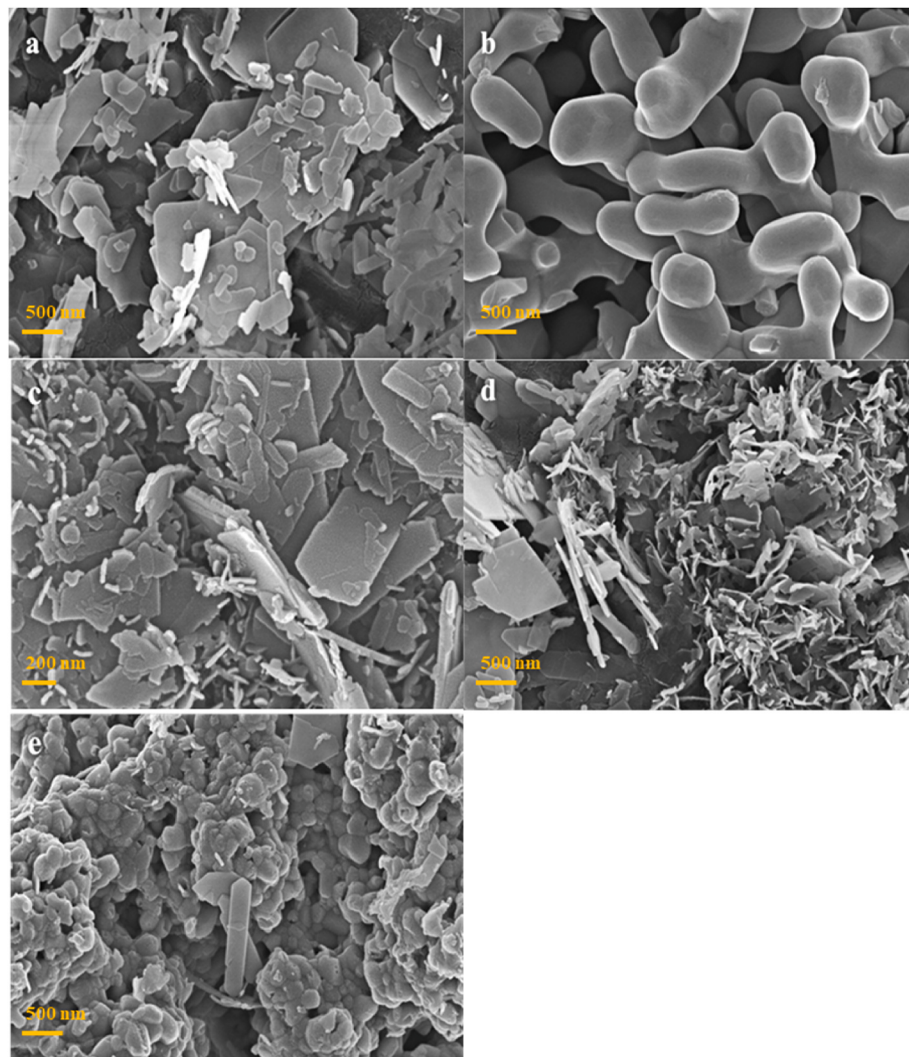


**Fig. 2.** SEM images of (a)  $\text{BiOIO}_3$ , (b)  $\text{Bi}_2\text{O}_3$ , (c) YBB-0, (d) YBB-1 and (e) YBB-10 photocatalysts.

material, as shown in Fig. 3 (b). It can be clearly seen from the figure that the lattice stripe spacing of  $\text{BiOIO}_3$  and  $\text{Bi}_2\text{O}_3$  materials is 0.290, 0.319 and 0.407 nm, which correspond to the (002) plane of  $\text{BiOIO}_3$ , the (111) plane of  $\beta\text{-Bi}_2\text{O}_3$  and the (020) plane of  $\alpha\text{-Bi}_2\text{O}_3$ , respectively. It is consistent with the XRD characterization results, indicating that when 1 mol%  $\text{Yb}^{3+}$  ions are doped,  $\alpha\text{-Bi}_2\text{O}_3$ ,  $\beta\text{-Bi}_2\text{O}_3$  and  $\text{BiOIO}_3$  coexist and compound with each other to form a triple heterojunction. It provides strong evidence for exploring the transfer path of photogenerated electron hole pairs between semiconductors in the process of photocatalysis. In the sample element analysis shown in Fig. 3 (c), all elements are evenly distributed in the whole nanocomposite, which proves that the YBB sample has been successfully synthesized.

### 3.3. Surface characterization

X-ray photoelectron spectroscopy (XPS) was used to characterize the valence and binding states of the elements in the samples. The XPS spectra of  $\text{BiOIO}_3$  nanosheets,  $\text{Bi}_2\text{O}_3$  nanoparticles and YBB-1 composite are shown in Fig. 4. The full XPS spectra of YBB-1 was showed in Fig. 4 (a). Bi, O, I and Yb elements were detected in the nanocomposites, indicating that the samples were successfully prepared, which further provided evidence for the coupling of  $\text{BiOIO}_3$  and  $\text{Bi}_2\text{O}_3$ . The characteristic peak of carbon element is due to detection error, and the C 1 peak with a binding energy of 284.6 eV is used for calibration [32], so only the peaks of Bi, I, O, and Yb need to be considered. Fig. 4 (b)–(e) extend

the high-resolution spectra of Bi 4f, I 3d, O 1s and Yb 4d. In Fig. 4 (b), the Bi 4f spectrum of YBB-1 has two characteristic peaks,  $\text{Bi } 4f_{7/2}$  and  $\text{Bi } 4f_{5/2}$ , corresponding to 159.0 eV and 164.3 eV, respectively, which is consistent with the chemical state of  $\text{Bi}^{3+}$  in  $\text{BiOIO}_3$  and  $\text{Bi}_2\text{O}_3$  [33]. Fig. 4 (c) shows the pattern of I 3d. The dominant peaks at 623.7 eV and 635.2 eV correspond to the  $\text{I } 3d_{5/2}$  and  $\text{I } 3d_{3/2}$  orbitals of  $\text{I}^{5+}$  in  $\text{BiOIO}_3$  [34], while the peaks at 618.8 eV and 630.5 eV are attributed to the contribution of  $\text{I}^-$ . It shows that part of  $\text{I}^{5+}$  is reduced to  $\text{I}^-$  in the preparation process, which proves that there are interactions between  $\text{BiOIO}_3$  nanosheets and  $\text{Bi}_2\text{O}_3$  nanoparticles. The O 1s spectrum can have three independent peaks at 529.3, 529.9 and 531.1 eV, respectively. The peaks at 529.3 and 529.9 eV denoted the lattice oxide in  $\text{Bi}-\text{O}$  and  $\text{I}-\text{O}$  bonds, respectively. The surface absorbed oxygen ( $-\text{OH}$  group and chemisorbed oxygen-containing species) corresponds to the peak located at 531.1 eV (Fig. 4d). The  $\text{Yb}^{3+}$  peak appeared at 184.1 eV (Fig. 4e). Compared with the original  $\text{BiOIO}_3$  and  $\text{Bi}_2\text{O}_3$ , the binding energies of Bi, I and O in YBB-1 move towards the direction of high binding energy, which indicates that  $\text{BiOIO}_3$ - $\text{Bi}_2\text{O}_3$  indeed interacts at the composite interface.

The specific surface area, pore volume and pore size of a photocatalyst affect its catalytic performance, so the Brunauer-Emmett-Teller (BET) method was carried out. As shown in Fig. 5a, the specific surface area of the sample was measured by the  $\text{N}_2$  adsorption-desorption isotherm method to verify the adsorption performance of the catalyst. All the isotherms belong to type IV and H3 hysteresis loops existed,

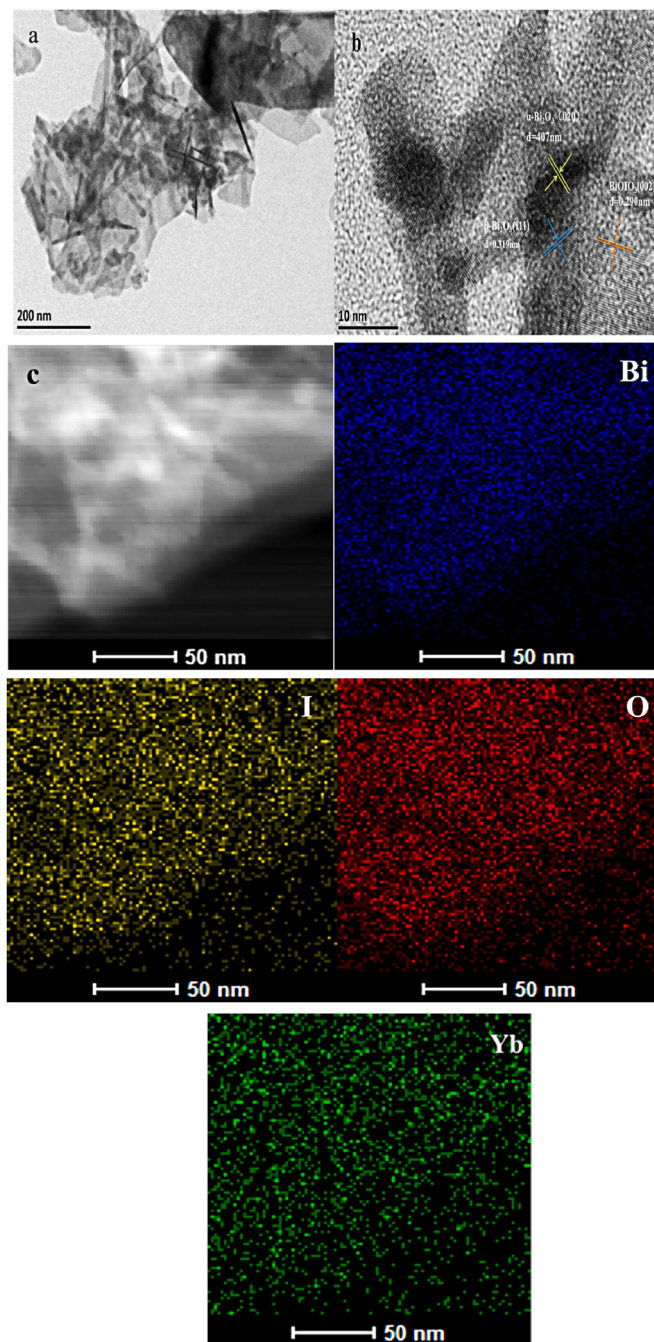


**Fig. 3.** (a) TEM, (b) HRTEM and (c) TEM maps of corresponding elements of YBB-1.

verifying their mesoporous characteristics [35], which could promote the photocatalytic oxidation reaction on the surface of a photocatalyst. The specific surface areas of  $\text{Bi}\text{IO}_3$ ,  $\text{Bi}_2\text{O}_3$ , YBB-0, YBB-1 and YBB-10 were calculated by BET formula. As shown in Table 1, the specific surface area values were 20.14, 39.20, 11.38, 11.50 and 11.23  $\text{m}^2/\text{g}$ , respectively. Obviously, the specific surface area of the composite sample decreases with the increase of the  $\text{Yb}^{3+}$  molar ratio, among which YBB-1 has the largest specific surface area in the composite sample, and the large specific surface area of the YBB-X composite can promote the photocatalytic reaction. The specific surface area of YBB-0 in the composite sample is the smallest and smaller than that of the pure sample, which can be attributed to the agglomeration of nanocomposites due to the calcination of the composite sample. The specific surface area may affect the catalytic oxidation performance, but it is not

the decisive factor, so it needs to be further analyzed with other characterizations.

### 3.4. Optical properties

As we all know, the light absorption capacity of a photocatalyst is an important factor affecting its photocatalytic performance. Fig. 5 (b) depicts the UV-Vis DRS spectrums of the composite samples. The absorption edges of  $\text{Bi}\text{IO}_3$  and  $\text{Bi}_2\text{O}_3$  nanoplates are about 400 nm and 468 nm, respectively, indicating that the response spectra of  $\text{Bi}_2\text{O}_3$  and  $\text{Bi}\text{IO}_3$  ranged from ultraviolet to part of visible light. YBB-0, YBB-1 and YBB-10 have a wide absorption tail at 400–612 nm. The absorption boundaries of YBB-0, YBB-1 and YBB-10 are 488, 600 and 612 nm, respectively. Compared with the pure sample, the absorption edge has a significant red shift, indicating that  $\text{Bi}_2\text{O}_3$  and  $\text{Bi}\text{IO}_3$  are successfully compounded and the band gap energy is reduced. YBB-1 and YBB-10 have large absorption cross sections in the range of 850–1100 nm, overlapping with one of the maximum near-infrared energy distributions of sunlight. Among them, the absorption peak at 980 nm is the highest, which just corresponds to the absorption of  $\text{Yb}^{3+}$ , further proving that the sample preparation is successful [36].

In order to further verify the optical properties of nanocomposites, the band gap energy ( $E_g$ ) of photocatalysts was calculated.

The band gap energy ( $E_g$ ) of the prepared samples can be estimated according to equations (2) and (3):

$$E_g = \frac{1240}{\lambda_{\text{Absorp. Edge}}} \quad (2)$$

$$\alpha h\nu = A(h\nu - E_g)^{\frac{n}{2}} \quad (3)$$

where  $E_g$ ,  $\alpha$ ,  $h\nu$  and  $A$  denote band gap, absorption coefficient, photon energy and constant, respectively.  $\text{Bi}\text{IO}_3$  is an indirect transition semiconductor,  $n = 4$ .  $\text{Bi}_2\text{O}_3$  is a direct semiconductor,  $n = 2$ . The band gap ( $E_g$ ) of  $\text{Bi}\text{IO}_3$  and  $\text{Bi}_2\text{O}_3$  can be estimated from the relative photon energy diagram. The tangent intercept is  $E_g$  of  $\text{Bi}\text{IO}_3$  and  $\text{Bi}_2\text{O}_3$ , as shown in Fig. 5c–d, with values of 3.0 eV and 2.85 eV, respectively. Although pure  $\text{Bi}\text{IO}_3$  is easy to transfer  $e^-$  to the (001) plane along the Z-axis in an electric field, it still faces a large recombination rate of  $e^-$  and  $h^+$ . The recombination and generation of electron-hole pairs cancel each other out, resulting in a reduction of the efficiency of the photocatalyst. However, the band gaps of the composites are lower than those of the two. From the subsequent DFT study, it can be seen that  $\text{Yb}^{3+}$  doping provides an impurity level for  $\text{Bi}_2\text{O}_3$ , thereby reducing the total band gap. Therefore, the higher reaction efficiency is due to their excellent separation ability of photogenerated electron-hole pairs. Secondly, the impurity level reduces the total band gap and increases the optical absorption boundary.

The separated electrons and holes combine with a hydroxyl group and oxygen to form an active component to enhance photocatalytic performance. Therefore, the performance of photocatalyst is highly dependent on the separation ability of photogenerated electrons and holes. Photoluminescence spectroscopy (PL) is a general method for characterizing the separation ability of photogenerated electrons and holes. In PL spectrum, the lower the peak intensity, the lower the recombination efficiency of electrons and holes. PL spectrum is shown in Fig. 5 (e). The fluorescence intensity of YBB-0, YBB-1 and YBB-10 is significantly lower than that of pure  $\text{Bi}\text{IO}_3$  and  $\text{Bi}_2\text{O}_3$ . YBB-1 shows the lowest emission intensity, so YBB-1 has the lowest electron-hole recombination efficiency. In addition, the peak value is about 455 nm, which explains that the triple heterojunction caused by  $\text{Bi}\text{IO}_3$  and  $\text{Bi}_2\text{O}_3$  greatly delays the recombination of photogenerated electron-hole pairs and improves the photocatalytic activity.

Then, the efficiency of electron-hole separation of composite materials was further studied by using Electrochemical impedance (EIS) and photoelectric current response. As shown in Fig. 5 (f), YBB-1 has the

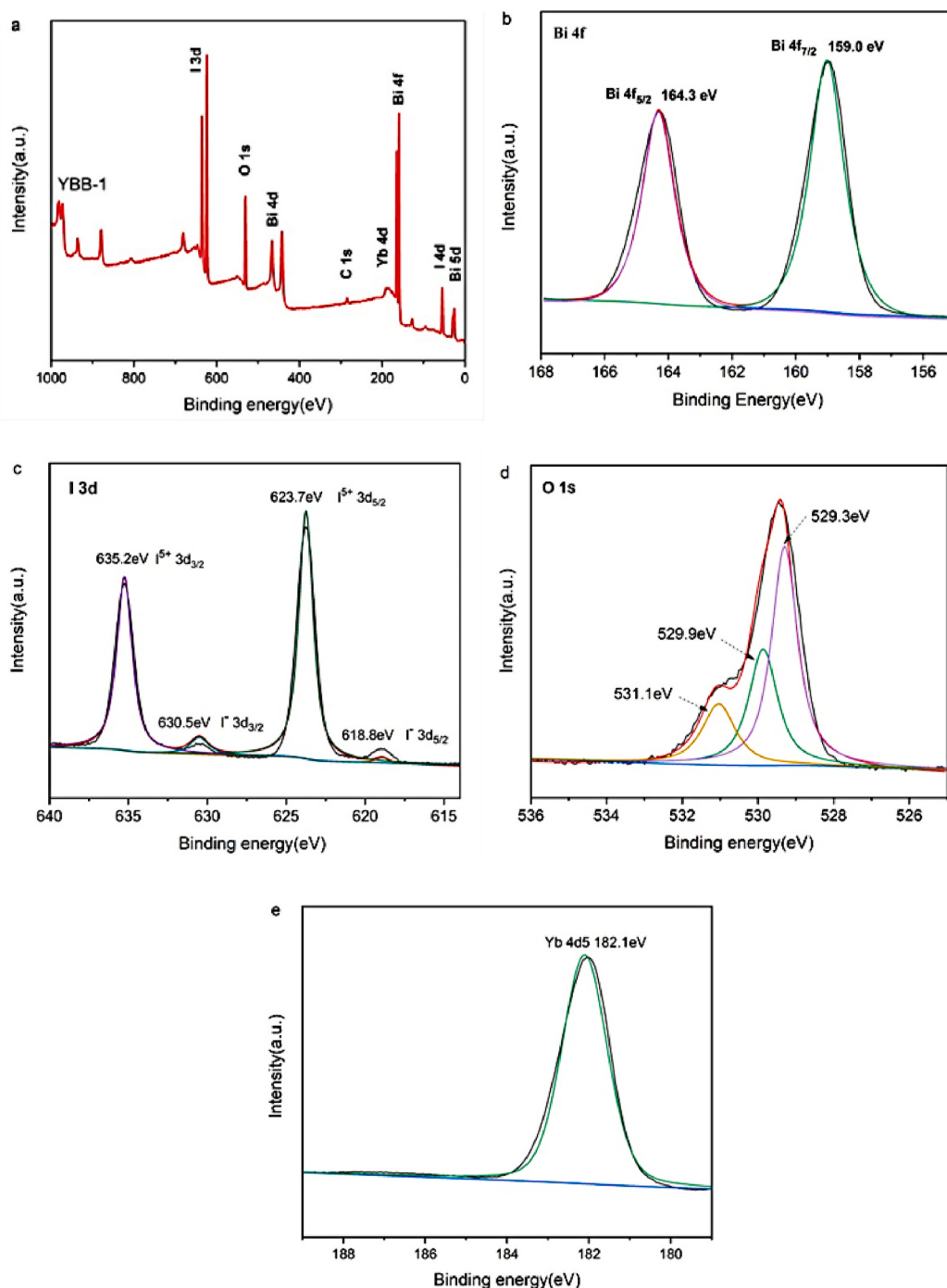


**Fig. 4.** (a) XPS full spectrum and element spectrum of YBB-1 (b) Bi 4f, (c) O 1s, (d) I 3d, (E) Yb 4d.

smallest radius of arc, which indicates that the interface resistance is lower than that of other samples, which is conducive to the separation and migration of charge. Fig. 5 (g) shows the transient photocurrent responses of BiOIO<sub>3</sub>, Bi<sub>2</sub>O<sub>3</sub>, YBB, YBB-1 and YBB-10, and the generally higher photocurrent density represents a better charge separation. The photocurrent response of the prepared sample is cycled four times under visible light. It can be seen that after turning on the light and turning off the light, the transient photocurrent of the sample increases and then decreases immediately, showing good photocurrent reproducibility, among which YBB-1 has the largest photocurrent density. It may be due to the joint action of rare earth ion doping and triple heterojunction. In conclusion, the electrochemical impedance and photocurrent response

show that YBB-1 has the best photochemical properties.

### 3.5. Photocatalytic performance

The Hg<sup>0</sup> removal experiment was carried out under the 24 W LED light ( $\lambda < 400$  nm) of visible light. The experiment was divided into three stages and lasted 70 min. In the first part of 15 min, because the specific surface area of the catalyst changes greatly, the influence of adsorption must be considered. The second part is the most important part of the whole experiment. Open the visible light source for 40 min to completely remove Hg<sup>0</sup> pollutants through photocatalysis. In the last stage, the stabilization process is reached 15 min after the lights are

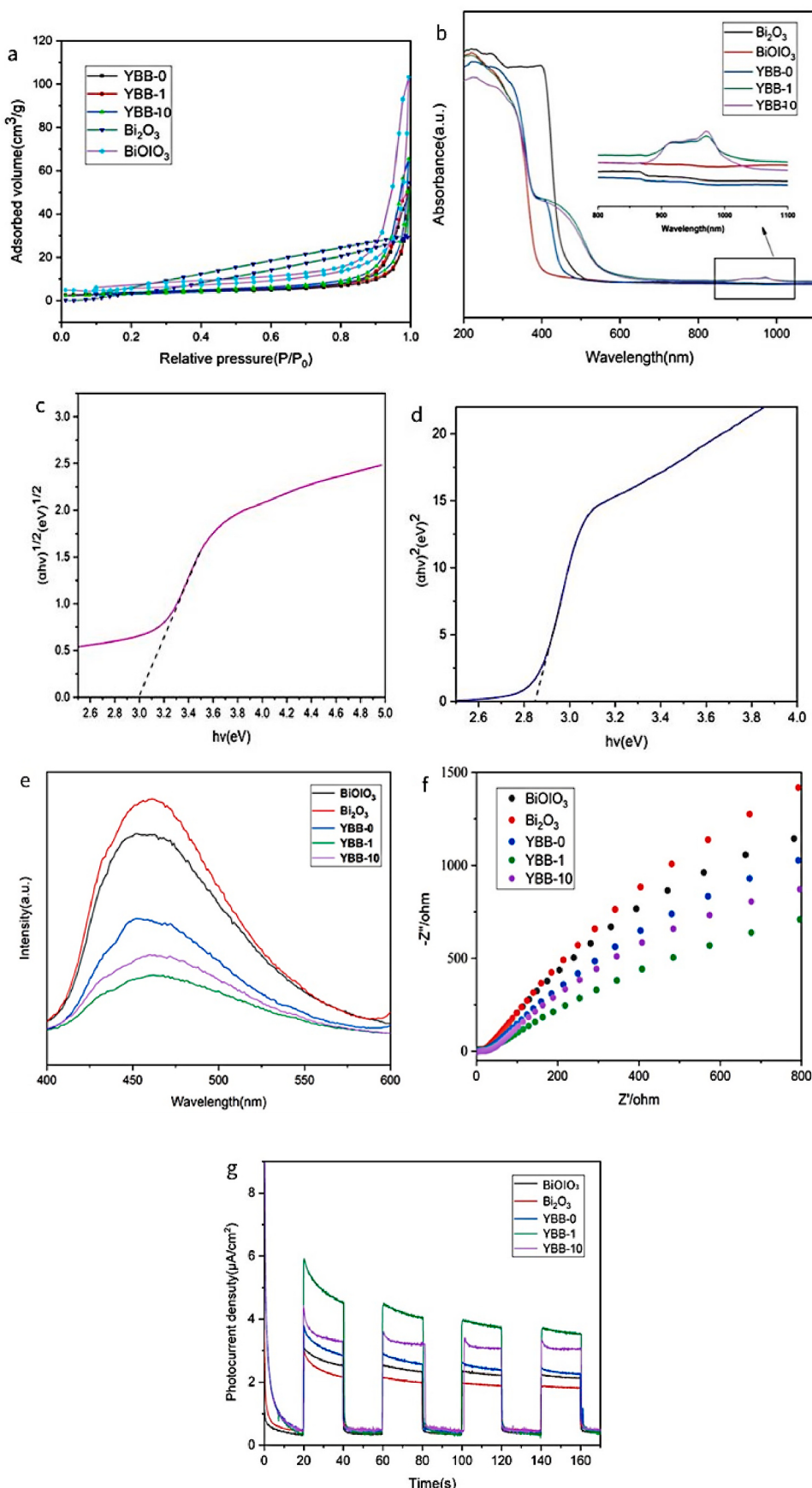


**Fig. 5.** (a) N<sub>2</sub> adsorption-desorption isotherms of BiOIO<sub>3</sub>, Bi<sub>2</sub>O<sub>3</sub>, YBB-0, YBB-1 and YBB-10.

**Table 1**

Physical properties and photocatalytic mercury removal efficiency of  $\text{BiOIO}_3$ ,  $\text{Bi}_2\text{O}_3$ , YBB-0, YBB-1 and YBB-10.

Sample	BET Surface Area ( $\text{m}^2/\text{g}$ )	Pore Volume ( $\text{cm}^3/\text{g}$ )	Pore Size (nm)
YBB-0	11.3846	0.075207	14.0805
YBB-1	11.4965	0.080337	14.8904
YBB-10	11.2277	0.049413	17.6038
$\text{Bi}_2\text{O}_3$	39.1974	0.044527	4.5439
$\text{BiOIO}_3$	20.1372	0.083724	16.6308

turned off. The overall photocatalytic reaction efficiency is shown in Fig. 6 (a) below. It can be seen from the figure that the mercury removal efficiency of YBB-0, YBB-1, YBB-10,  $\text{BiOIO}_3$  and  $\text{Bi}_2\text{O}_3$  is 57.51%, 76.73%, 67.58%, 54.43% and 39.35%, respectively. All of them are much more efficient than the standard catalyst P25 reported before [31]. The mercury removal efficiency of composite photocatalysis is higher than that of a single catalyst, which indicates that the two substances are successfully combined to form a heterojunction. The doping of  $\text{Yb}^{3+}$  makes  $\text{Bi}_2\text{O}_3$  undergo phase transition. In YBB-0, only  $\alpha\text{-Bi}_2\text{O}_3$  and  $\text{BiOIO}_3$  compounds form a common single heterostructure, which can promote the separation of photogenerated electron hole pairs in YBB-1,

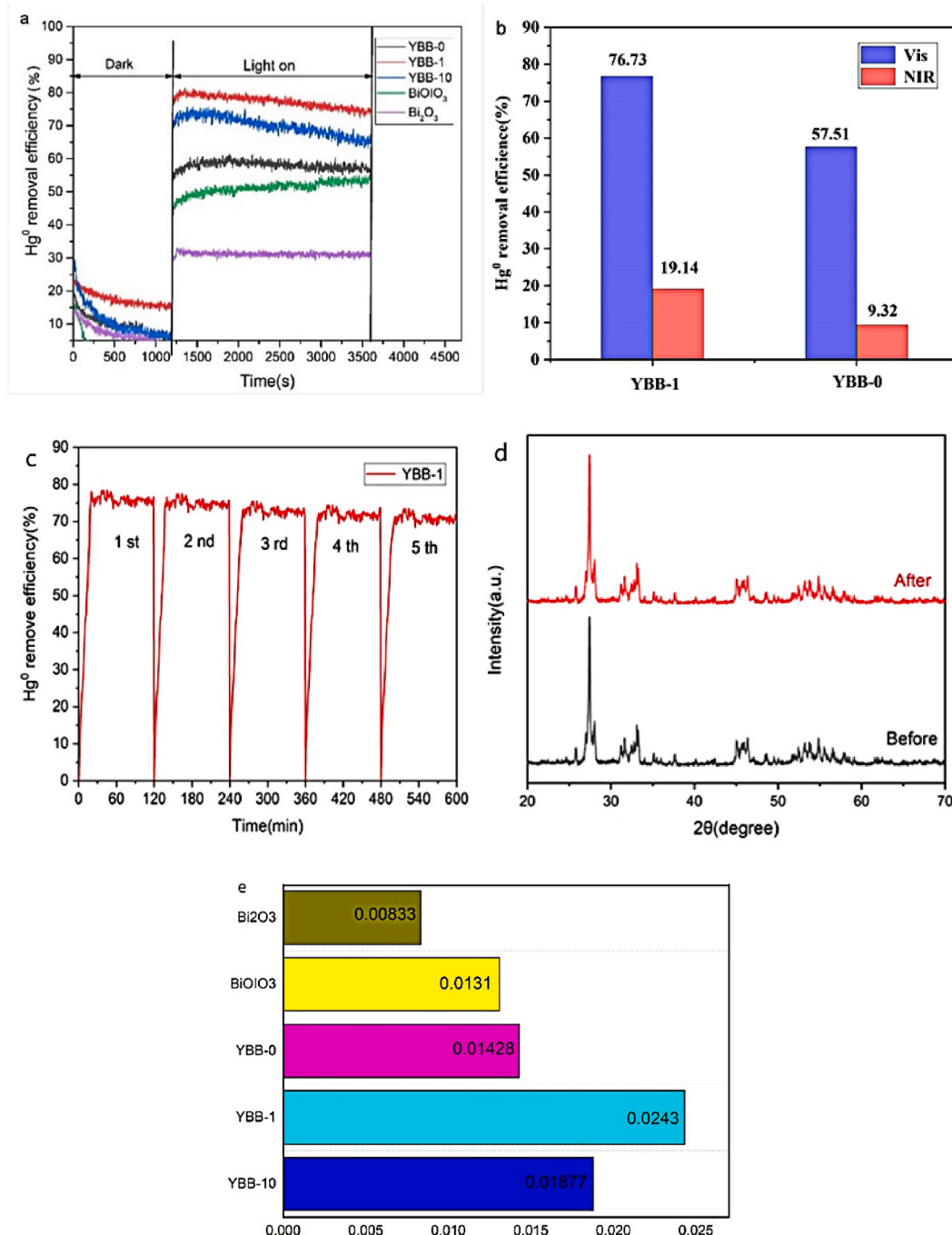


**Fig. 6.** (a) Mercury removal efficiency of composite photocatalyst under dark and LED light; (b) photocatalytic mercury removal efficiency of YBB-1 and YBB-0 under Vis-NIR; (c) diagram of circulating mercury removal efficiency; (d) XRD comparison diagram before and after use of YBB-1 composite photocatalyst; (e) Kinetics of  $\text{Hg}^0$  oxidation reaction over the  $\text{BiOIO}_3$ ,  $\text{Bi}_2\text{O}_3$ , YBB-0, YBB-1 and YBB-10 samples.

$\alpha\text{-Bi}_2\text{O}_3$  and  $\beta\text{-Bi}_2\text{O}_3$  crystal phases coexist with bismuth trioxide, and the three combine to form a triple heterostructure, which constructs a more complex electronic transmission channel. However,  $\alpha\text{-Bi}_2\text{O}_3$  in YBB-10 is completely converted to  $\beta\text{-Bi}_2\text{O}_3$ , and a single heterostructure is restored, which reduces the photocatalytic efficiency. In addition, Fig. 6 (b) further describes the mercury removal efficiency of YBB-1 and YBB-0 photocatalysts under near-infrared radiation. The mercury removal efficiency of  $\text{Yb}^{3+}$  doped composite photocatalyst YBB-1 under infrared light is twice as high as that of  $\text{Yb}^{3+}$  doped composite photocatalyst YBB-0. This is due to the unique electronic transition characteristics of  $\text{Yb}^{3+}$ , which broadens the spectral response range of the composite photocatalyst and improves the photocatalytic performance.

In order to further intuitively compare the reaction kinetics of  $\text{Hg}^0$  photocatalytic oxidation, the Langmuir Hinshelwood pseudo first order

reaction model was studied [36,37]:

$$-\ln\left(\frac{C}{C_0}\right) = kt \quad (4)$$

where  $C_0$  and  $C$  represented inlet and outlet gas-phase  $\text{Hg}^0$  concentration ( $\mu\text{g}/\text{m}^3$ ),  $k$  and  $t$  represented pseudo-first-order rate constant ( $\text{min}^{-1}$ ) and reaction time. Hence, as displayed in Fig. 6 (e), for YBB-0, YBB-1, YBB-10,  $\text{BiOIO}_3$  and  $\text{Bi}_2\text{O}_3$ , the reaction rate constant was determined to be 0.01428, 0.02430, 0.018773, 0.013098 and 0.008334  $\text{min}^{-1}$ , respectively. The highest photocatalytic reaction rate of YBB-1 is about 3 times that of  $\text{Bi}_2\text{O}_3$  and 2 times that of  $\text{BiOIO}_3$ , which further proves that YBB-1 has better photocatalytic performance than other samples.

The stability of the photocatalyst is an important factor affecting its

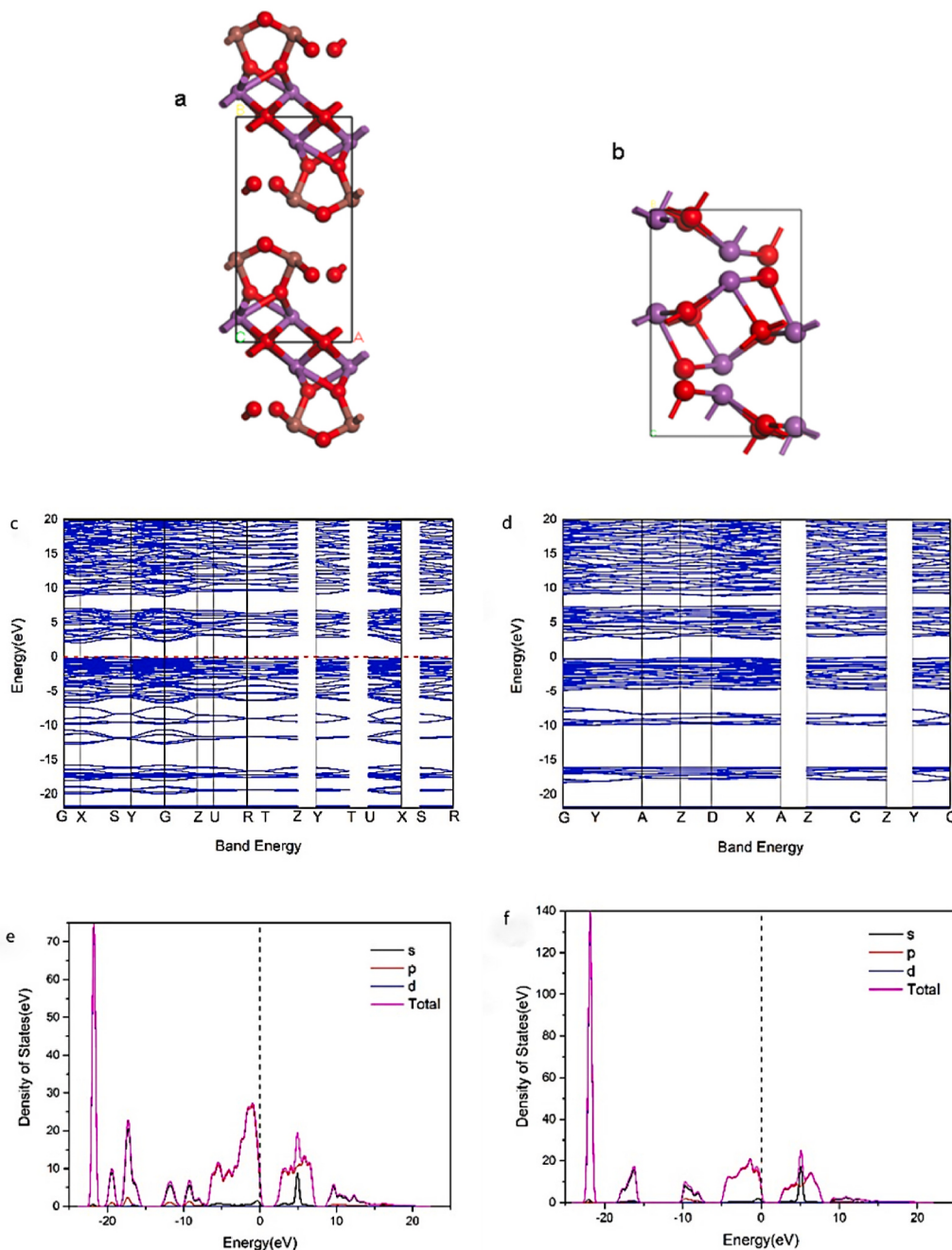


**Fig. 7.** The geometrically optimized structures of (a)  $\text{BiOIO}_3$  and (b)  $\alpha\text{-Bi}_2\text{O}_3$ ; Band structure of (c)  $\text{BiOIO}_3$  and (d) $\alpha\text{-Bi}_2\text{O}_3$ ; Density of states (DOS) of (e)  $\text{BiOIO}_3$  and (f) $\alpha\text{-Bi}_2\text{O}_3$ .

practical application. The photocatalytic stability of YBB-1 samples was tested by the cyclic photocatalytic oxidation of  $\text{Hg}^0$ . Each cyclic experiment was carried out under the same conditions. First, the sample was placed in the dark for 30 min, then the quartz glass coated with YBB-1 sample was placed under the LED lamp for 90 min, the LED lamp was turned off, and then the  $\text{Hg}^0$  concentration reached a stable value. About 30 min later, the next cycle experiment was carried out in the same steps. After five cycles of experiments, it can be seen from Fig. 6 (c) that the mercury removal efficiency changed from 76.7% to 71.2%, only about 5% decreased. At the same time, the photocatalyst after five cycles was characterized by XRD. It can be seen from Fig. 6 (d) that the sample atlas has almost no change, indicating that the composite photocatalyst has good stability and chemical durability.

### 3.6. Reaction mechanism

#### 3.6.1. Theoretical calculation

According to the above characterization of physical and chemical properties and the experiment of mercury removal by photocatalytic oxidation, it can be determined that YBB-1 has the best photocatalytic performance. The possible mechanism of improving photocatalytic activity was further explained by density functional theory (DFT) calculation. Fig. 7 (a) - (b) shows the geometric optimization structure of  $\text{BiOIO}_3$  and  $\alpha\text{-Bi}_2\text{O}_3$ . Band gap is the potential difference between the maximum value of the valence band (VB) and the minimum value of the conduction band (CB), which has an important impact on the photoelectric performance of catalysts [34]. Therefore, we simulated the band gap structure of the catalyst by CASTEP calculation. In Fig. 7 (c)-(d), it is calculated that the band structures of  $\text{BiOIO}_3$  and  $\alpha\text{-Bi}_2\text{O}_3$  are 1.961 and 2.376 eV respectively, which is slightly different from the experimental calculation value. It can be attributed to the calculation error of the GGA

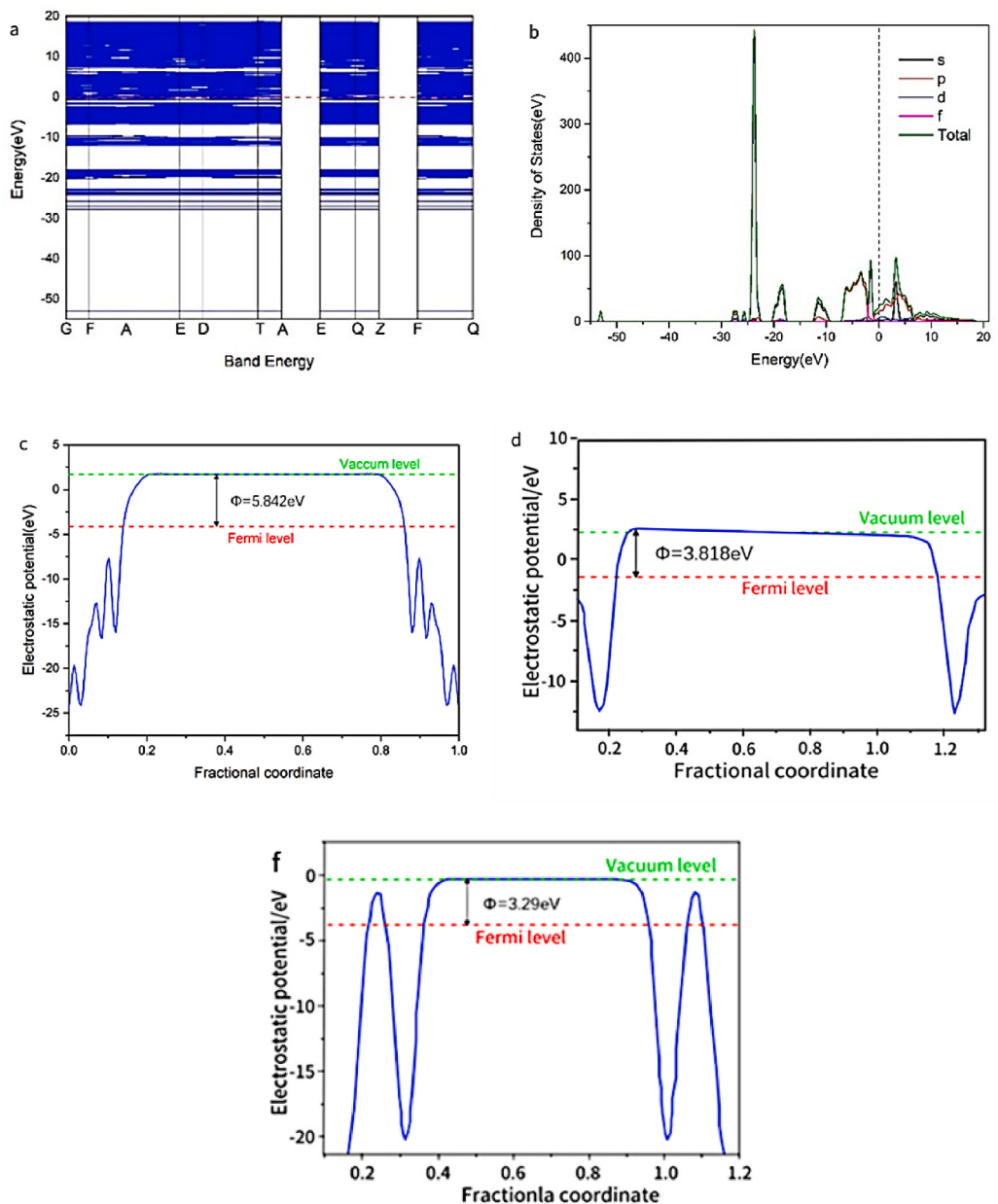


**Fig. 8.** (a) Band structure of  $\text{Bi}_2\text{O}_3$  doped with  $\text{Yb}^{3+}$ , (b) density of states (DOS) of  $\text{Bi}_2\text{O}_3$  doped with  $\text{Yb}^{3+}$ , Electrostatic potentials of (c) $\text{BiOIO}_3$ (010), (d) $\alpha\text{-Bi}_2\text{O}_3$ (001) and (e) $\beta\text{-Bi}_2\text{O}_3$ (111) planes.

functional that usually underestimates the band gap [34,38]. Simultaneously, the density of states (DOS) of  $\text{BiOIO}_3$  and  $\alpha\text{-Bi}_2\text{O}_3$  were calculated, and the results are shown in Fig. 7 (e)–(f). It can be observed from Fig. 7 (e) that in the case of  $\text{BiOIO}_3$  bulk, the VB was predominately composed of O 2p states, and the bottom of CB was made up of Bi 6p states, O 2p states, and I 5p states. The results are consistent with previous literature on  $\text{BiOIO}_3$  [39,40]. In Fig. 7 (f), it can be seen that the VB is mainly derived from the O 2p orbitals in the case of  $\alpha\text{-Bi}_2\text{O}_3$  bulk, whereas the CB is mainly derived from the Bi 6p orbitals, which is consistent with the results of previous studies [41,42].

Compared with pure  $\text{Bi}_2\text{O}_3$ ,  $\text{Yb}^{3+}$  doped can effectively reduce the band gap of  $\text{Bi}_2\text{O}_3$  by generating impurity energy levels, which may lead to more light absorption (Fig. 8 (a)). It is consistent with the results of UV-Vis NIR spectra in Fig. 7. From the detailed  $\text{Yb}^{3+}$  doped DOS spectrum shown in Fig. 8 (b), it can be seen that VBM still mainly comes from the O 2p orbital. The CBM is mainly composed of Bi 6p and Yb 4f orbitals, while the new impurity band is mainly contributed by Yb 4f orbitals and a small amount of O 2p orbitals. The results show that  $\text{Yb}^{3+}$  doping can induce O 2p orbitals to produce impurity energy levels in the band gap of  $\text{Bi}_2\text{O}_3$ , and then reduce the band gap, resulting in the phase transition of  $\text{Bi}_2\text{O}_3$ , further promoting the separation of photogenerated electron-hole pairs. It is beneficial to photocatalytic performance.

The surface work functions of  $\text{BiOIO}_3(010)$  [43],  $\alpha\text{-Bi}_2\text{O}_3(001)$  [44] and  $\beta\text{-Bi}_2\text{O}_3(111)$  [45] planes were calculated by CASTEP using density functional theory, so as to reveal the interface transfer between them more deeply [46]. The work functions of  $\text{BiOIO}_3(010)$ ,  $\alpha\text{-Bi}_2\text{O}_3(001)$  and  $\beta\text{-Bi}_2\text{O}_3(111)$  are calculated according to the following equation:

$$\Phi = E_{\text{vac}} - E_F \quad (5)$$

Where  $E_{\text{vac}}$  is the electrostatic potential at the vacuum level and  $E_F$  is the fermi energy [47]. The electrostatic potentials of  $\text{BiOIO}_3(010)$ ,  $\alpha\text{-Bi}_2\text{O}_3(001)$ , and  $\beta\text{-Bi}_2\text{O}_3(111)$  planes are shown in Fig. 8 (c)–(e). We calculated and attained the work functions of  $\text{BiOIO}_3(010)$ ,  $\alpha\text{-Bi}_2\text{O}_3(001)$  and  $\beta\text{-Bi}_2\text{O}_3(111)$  planes, which are 5.842, 3.818 and 3.29 eV, respectively. This indicates that there is charge transport at the interface between the three semiconductors. The charge can be transferred from  $\text{BiOIO}_3$  with a higher work function to  $\text{Bi}_2\text{O}_3$  with a lower work function. At the same time, between different crystal phases of  $\text{Bi}_2\text{O}_3$ , the charge is transferred from  $\alpha\text{-Bi}_2\text{O}_3$  with a higher work function to  $\beta\text{-Bi}_2\text{O}_3$  with a lower work function. Finally, the Fermi energy levels will be equal [48]. The high work function results in the loss of electrons at the interface to obtain holes, which are positively charged. The low work function electrons lose holes and are negatively charged. Therefore, the interface heterojunction of  $\text{BiOIO}_3$  and  $\alpha\text{-Bi}_2\text{O}_3$ , the interface heterojunction of  $\text{BiOIO}_3$  and  $\beta\text{-Bi}_2\text{O}_3$ , and the interface homojunction of  $\alpha\text{-Bi}_2\text{O}_3$  and  $\beta\text{-Bi}_2\text{O}_3$  form three progressive internal electric fields respectively, accelerating the separation and transmission of charge carriers [46]. Due to the loss of electrons, the energy band edges of  $\text{BiOIO}_3$  and  $\alpha\text{-Bi}_2\text{O}_3$  at the interface bend upward. Due to the accumulation of electrons, the energy band edges of  $\beta\text{-Bi}_2\text{O}_3$  at the interface bend downward, which further effectively inhibits the recombination of photogenerated carriers [49]. In conclusion, the band bending and built-in electric field at the interface of  $\text{BiOIO}_3$ ,  $\alpha\text{-Bi}_2\text{O}_3$  and  $\beta\text{-Bi}_2\text{O}_3$  promote charge transfer, and maintain the high reducibility of  $\beta\text{-Bi}_2\text{O}_3$  and the high oxidation capacity of  $\text{BiOIO}_3$  [46].

### 3.6.2. Charge transfer

The electron spin resonance (ESR) technology of DMPO was used to

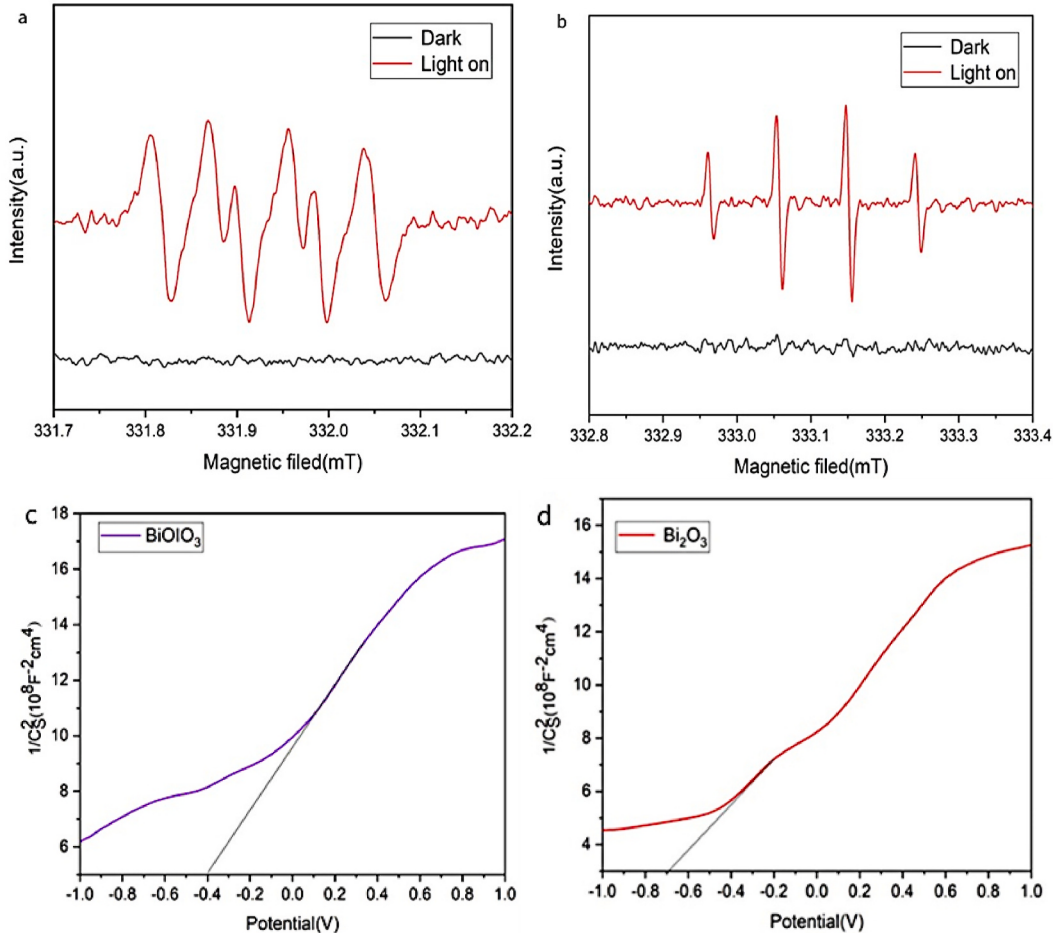


Fig. 9. ESR spectrum of composite photocatalyst YBB-1 (a) DMPO ·O<sub>2</sub><sup>-</sup> and (b) DMPO ·OH, Mott-Schott curves of (c)  $\text{BiOIO}_3$  and (d)  $\text{Bi}_2\text{O}_3$ .

test the reactivity of YBB-1 under dark and visible light conditions, and to study the substances that play an important role in mercury removal under visible light. As shown in Fig. 9 (a),  $\bullet\text{O}_2^-$  and  $\bullet\text{OH}$  ESR signals are not generated in the dark. A group of six spectral peaks were observed under visible light, which were specific signal peaks of DMPO- $\bullet\text{O}_2^-$ . This means that  $\text{O}_2$  on the catalyst surface is reduced to  $\bullet\text{O}_2^-$  by electrons. Similarly, by dispersing the photocatalyst in water, a strong DMPO- $\bullet\text{OH}$  signal of 1:2:2:1 can be observed, indicating that  $\bullet\text{OH}$  is formed on the surface of the composite catalyst. Therefore, the above experimental results show that  $\bullet\text{O}_2^-$  and  $\bullet\text{OH}$  are mainly responsible for the photocatalytic oxidation of gaseous  $\text{Hg}^0$ .

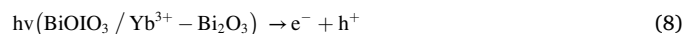
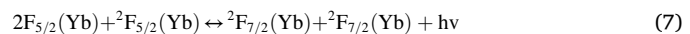
In addition, the flat band potential ( $E_{fb}$ ) of  $\text{BiOIO}_3$  and  $\text{Bi}_2\text{O}_3$  is further measured by using the Mott-Schottky curve. The positive slope of the Mott-Schottky curve in Fig. 9 (c)-(d) indicates that  $\text{BiOIO}_3$  and  $\text{Bi}_2\text{O}_3$  are both n-type semiconductors. It can be seen from the figure that the flat band potential ( $E_{fb}$ ) of  $\text{BiOIO}_3$  and  $\text{Bi}_2\text{O}_3$  are  $-0.69\text{ eV}$  and  $-0.46\text{ eV}$ , respectively. Because the value calculated by the formula is close to the conduction band value, and it is often equal to the conduction band potential ( $E_{CB}$ ) of the material, so the CB of  $\text{BiOIO}_3$  and  $\text{Bi}_2\text{O}_3$  are  $-0.69\text{ eV}$  and  $-0.46\text{ eV}$  respectively. According to equation (6), the VB values of  $\text{BiOIO}_3$  and  $\text{Bi}_2\text{O}_3$  are  $2.31\text{ eV}$  and  $2.39\text{ eV}$ , respectively. When  $\text{Yb}^{3+}$  is doped with  $\text{Bi}_2\text{O}_3$ ,  $\text{Yb}^{3+}$  will replace  $\text{Bi}^{3+}$  in  $\text{Bi}_2\text{O}_3$ , resulting in phase transition of impurity energy level generated by  $\text{Bi}_2\text{O}_3$ . Therefore, the CB and VB of  $\beta\text{-Bi}_2\text{O}_3$  will be lower than that of  $\alpha\text{-Bi}_2\text{O}_3$ .

$$E_{CB} = E_{VB} - E_g \quad (6)$$

The possible mechanism of photocatalytic reduction of  $\text{Hg}^0$  is shown in Fig. 10. It can be seen from the figure that the conduction band position sequence is  $\text{BiOIO}_3 > \alpha\text{-Bi}_2\text{O}_3 > \beta\text{-Bi}_2\text{O}_3$ . When visible light shines on YBB-1,  $\text{BiOIO}_3$  is first excited. The  $\text{h}^+$  stay on VB. The  $e^-$  on the CB is directly transferred to the CB of  $\beta\text{-Bi}_2\text{O}_3$  or transferred to the CB of  $\beta\text{-Bi}_2\text{O}_3$  through  $\alpha\text{-Bi}_2\text{O}_3$ . At the same time, the excited  $e^-$  on the CB of  $\alpha\text{-Bi}_2\text{O}_3$  is also transferred to the CB of adjacent  $\beta\text{-Bi}_2\text{O}_3$ . Similarly,  $\text{h}^+$  moves to the VB of  $\text{BiOIO}_3$  in the opposite path. Finally, the CB of  $\beta\text{-Bi}_2\text{O}_3$  converges  $e^-$ , and the VB of  $\text{BiOIO}_3$  converges  $\text{h}^+$ . Based on the construction of its complex electron transport orbit, the recombination rate of photogenerated electrons and holes is greatly hindered, even almost no recombination. Since  $\text{O}_2/\cdot\text{O}_2^- (-0.28\text{ eV})$  is greater than  $e^- (-0.46\text{ eV})$ , the photogenerated electrons on the CB of  $\text{Bi}_2\text{O}_3$  can easily reduce  $\text{O}_2$  to strong oxidizing  $\cdot\text{O}_2^-$  ions. Since  $\cdot\text{OH}/\text{OH}^- (+1.99\text{ eV})$  is less than  $\text{h}^+ (+2.31\text{ eV})$ ,  $\text{h}^+$  can oxidize  $\text{H}_2\text{O}$  and  $\text{OH}^-$  to  $\cdot\text{OH}$ , and these active oxygen clusters ( $\cdot\text{O}_2^-$  and  $\cdot\text{OH}$ ) can oxidize  $\text{Hg}^0$  to  $\text{HgO}$ . The

generated  $\text{HgO}$  can be well adsorbed on the catalyst surface for further removal.

All in all, when the doped  $\text{Yb}^{3+}$  is 1 mol%, the two crystal phases of  $\alpha\text{-Bi}_2\text{O}_3$  and  $\beta\text{-Bi}_2\text{O}_3$  coexist and form a triple heterostructure with  $\text{BiOIO}_3$ , which constructs a unique electron transport orbit and effectively promotes the separation of photogenerated electrons-hole pairs. At the same time,  $\text{Yb}^{3+}$  has unique electronic orbital transition characteristics, which can broaden the spectral response of composite photocatalysis and effectively improve the photocatalytic activity. The specific reaction process is as follows:



#### 4. Conclusions

In conclusion, we have successfully prepared a new ternary composite photocatalyst  $\text{Yb}^{3+}\text{-Bi}_2\text{O}_3/\text{BiOIO}_3$  with triple heterojunction and broad spectral absorption, and evaluated the sample through flue gas mercury removal experiment. DFT theoretical calculation was carried out at the same time of a series of characterization, which provided a basis for further study of the reaction mechanism. The results showed that YBB-1 had the best performance of photocatalytic removal of  $\text{Hg}^0$ , and the removal rate of  $\text{Hg}^0$  was 76.73%, compared with pure  $\text{Bi}_2\text{O}_3$ , pure  $\text{BiOIO}_3$ , YBB-0 and YBB-10. The doped of  $\text{Yb}^{3+}$  results in the coexistence of various crystal phases of  $\text{Bi}_2\text{O}_3$  and the formation of heterojunction with  $\text{BiOIO}_3$ , while giving play to its unique electronic transition characteristics. This provides a unique transmission channel

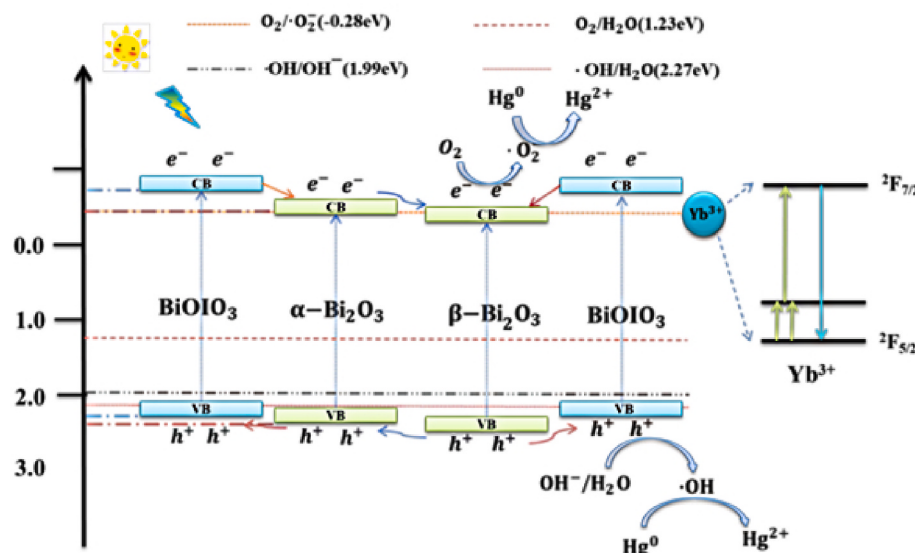


**Fig. 10.** Schematic diagram of charge transfer mechanism and photocatalytic mercury removal mechanism.

for photogenerated electrons-holes, and promotes the separation of photogenerated electrons and holes. At the same time, it greatly broadens the spectral response and improves the photocatalytic activity of the catalyst. Therefore, this work provides a new method for constructing more efficient photocatalysts.

### Credit author statement

Tong Li: Formal analysis, Writing - original draft, Writing - review & editing, Validation, Investigation. Siyuan Ren: Project administration, Supervision, Writing - review & editing, Jiang Wu: Conceptualization, Methodology, Software, Supervision, Funding acquisition, Project administration. Min Zhou: Resources, Data curation, Software. Cheng Peng: Resources, Data curation, Software. Hai Zhang: Resources, Data curation. Ping He: Resources, Data curation, Software. Xuemei Qi: Resources, Data curation, Validation. Mao Song: Resources, Data curation, Validation. Yuzhuo Zhou: Resources, Data curation, Validation, Visualization. Shuo Chen: Resources, Data curation, Writing - review.

**Table 1** Physical properties and photocatalytic mercury removal efficiency of BiOIO<sub>3</sub>, Bi<sub>2</sub>O<sub>3</sub>, YBB-0, YBB-1 and YBB-10; (b) UV–Vis DRS spectra of BiOIO<sub>3</sub>, Bi<sub>2</sub>O<sub>3</sub>, YBB-0, YBB-1 and YBB-10 photocatalysts; (xhv)<sup>(n/2)-hν</sup> curve of (c) BiOIO<sub>3</sub> and (d) Bi<sub>2</sub>O<sub>3</sub>; (e) PL, (f) EIS and (g) the transient photocurrent responses of BiOIO<sub>3</sub>, Bi<sub>2</sub>O<sub>3</sub>, YBB-0, YBB-1 and YBB-10 photocatalysts.

### Declaration of competing interest

The authors declare that they have no known competing financial interests or personal relationships that could have appeared to influence the work reported in this paper.

### Data availability

Data will be made available on request.

### Acknowledgments

This work was partially sponsored by National Natural Science Foundation of China (52076126), Science and Technology Committee of Shanghai Municipality (22010501500), and Key Laboratory of Clean Power Generation and Environmental Protection Technology in Mechanical Industry. The authors would like to thank Shiyanjia Lab (<http://www.shiyanjia.com/>) for the support of SEM, BET, and XPS test.

### Appendix A. Supplementary data

Supplementary data to this article can be found online at <https://doi.org/10.1016/j.solidstatesciences.2023.107151>.

### References

- [1] D.P. Krabbenhoft, E.M. Sunderland, Global change and mercury, *Science* (2013) 341.
- [2] L. Zhang, S.X. Wang, Q.R. Wu, F.Y. Wang, C.J. Lin, L.M. Zhang, M.L. Hui, M. Yang, H.T. Su, J.M. Hao, Mercury transformation and speciation in flue gases from anthropogenic emission sources: a critical review, *Atmos. Chem. Phys.* 16 (2016).
- [3] L.C. Barkay T, M. Gillman, Environmental significance of the potential for mer (Tn21)-mediated reduction of Hg<sup>2+</sup> to Hg<sup>0</sup> in natural waters, *Appl. Environ. Microbiol.* 55 (1989).
- [4] K.S.A.a.L.I.E. Bondarev I V, Dynamical tensor polarizability in the ground state of the hydrogen atom, *J. Phys. B-At. Mol. Opt.* 25 (1992).
- [5] H.Q. Yang, Z.H. Xu, M.H. Fan, A.E. Bland, R.R. Judkins, Adsorbents for capturing mercury in coal-fired boiler flue gas, *J. Hazard Mater.* 146 (2007).
- [6] J. Wu, P.F. Sheng, W.X. Xu, X. Zhou, C. Lu, Z. Ji, K. Xu, L. Zhu, X. Zhang, W. Feng, Constructing interfacial contact for enhanced photocatalytic activity through BiOIO<sub>3</sub>/g-C<sub>3</sub>N<sub>4</sub> nanoflake heterostructure, *Catal. Commun.* (109) (2018).
- [7] A. Phuruangrat, S. Wannapop, T. Sakhon, B. Kuntalue, T. Thongtem, S. Thongtem, Characterization and photocatalytic properties of BiVO<sub>4</sub> synthesized by combustion method, *J. Mol. Struct.* 1274 (2023).
- [8] S. Pinchujit, A. Phuruangrat, S. Wannapop, T. Sakhon, B. Kuntalue, T. Thongtem, S. Thongtem, Synthesis and characterization of heterostructure Pt/Bi<sub>2</sub>WO<sub>6</sub> nanocomposites with enhanced photodegradation efficiency induced by visible radiation, *Solid State Sci.* 134 (2022).
- [9] T.P. Thanh, R. Daiyan, Z. Fusco, Z.P. Ma, R. Amal, A. Tricoli, Nanostructured beta-Bi<sub>2</sub>O<sub>3</sub> fractals on carbon fibers for highly selective CO<sub>2</sub> electroreduction to formate, *Adv. Funct. Mater.* 30 (2020).
- [10] H.F. Cheng, B.B. Huang, Y. Dai, Engineering BiOX (X = Cl, Br, I) nanostructures for highly efficient photocatalytic applications, *Nanoscale* 6 (2014).
- [11] J. Di, J.X. Xia, H.M. Li, S.J. Guo, S. Dai, Bismuth oxyhalide layered materials for energy and environmental applications, *Nano Energy* 41 (2017).
- [12] H. Zhao, F. Tian, R. Wang, R. Chen, A review on bismuth-related nanomaterials for photocatalysis, *Rev. Adv. Sci. Eng.* 3 (2014).
- [13] X.M. Sun, J. Wu, Q.F. Li, Q.Z. Liu, Y.F. Qi, L. You, Z. Ji, P. He, P.F. Sheng, J.X. Ren, W.B. Zhang, J. Lu, J.J. Zhang, Fabrication of BiOIO<sub>3</sub> with Induced Oxygen Vacancies for Efficient Separation of the Electron-Hole Pairs, vol. 218, *Applied Catalysis B-Environmental*, 2017.
- [14] K. Xu, J. Wu, F.G. Tian, Q.Z. Liu, C.H. Qu, W.G. Pan, P. He, H. Muzvidiwa, Z. Zhang, Intensifying internal electric field for efficient charge separation in different dimensions photocatalysts via in-situ crystallization, *Mater. Lett.* (2018) 224.
- [15] Y.J. Sun, T. Xiong, F. Dong, H.W. Huang, W.L. Cen, Interlayer-I-doped BiOIO<sub>3</sub> nanoplates with an optimized electronic structure for efficient visible light photocatalysis, *Chem. Commun.* (2016) 52.
- [16] C. Zeng, Y.M. Hu, H.W. Huang, BiOBr<sub>0.75</sub>O<sub>2.25</sub>/BiOIO<sub>3</sub> as a novel heterojunctional photocatalyst with superior visible-light-driven photocatalytic activity in removing diverse industrial pollutants, *ACS Sustain. Chem. Eng.* 5 (2017).
- [17] Y.X. Xiao, S.Q. Tan, D.L. Wang, J. Wu, T. Jia, Q.Z. Liu, Y.F. Qi, X.M. Qi, P. He, M. Zhou, CeO<sub>2</sub>/BiOIO<sub>3</sub> Heterojunction with Oxygen Vacancies and Ce<sup>4+</sup>/Ce<sup>3+</sup> Redox Centers Synergistically Enhanced Photocatalytic Removal Heavy Metal, *Applied Surface Science*, 2020.
- [18] H.L. Liu, B. Wu, S.K. Wu, Y.S. Liu, S. Yoriya, C. Hu, H. Zhang, J. Wu, Y. Ling, P. He, X. Qi, Ion Doping Engineering of Nickel-Doped BiOIO<sub>3</sub> Nanosheets for Gaining Oxygen Vacancy to Enhance Light Absorption, *Fuel Processing Technology*, 2022.
- [19] W.W. Dai, Z.Y. Zhao, DFT study on the interfacial properties of vertical and in-plane BiOI/BiOIO<sub>3</sub> hetero-structures, *Phys. Chem. Chem. Phys.* 19 (2017).
- [20] S.Y. Yu, L. Zhang, L.B. Zhu, Y. Gao, G.C. Fan, D.M. Han, G.X. Chen, W.W. Zhao, Bismuth-containing semiconductors for photoelectrochemical sensing and biosensing, *Coord. Chem. Rev.* 393 (2019).
- [21] W. Raza, A. Khan, U. Alam, M. Muineer, D. Bahnamann, Facile fabrication of visible light induced Bi<sub>2</sub>O<sub>3</sub> nanorod using conventional heat treatment method, *J. Mol. Struct.* 1107 (2016).
- [22] O. Yayapao, T. Thongtem, A. Phuruangrat, S. Thongtem, Synthesis and characterization of highly efficient Gd doped ZnO photocatalyst irradiated with ultraviolet and visible radiations, *Mater. Sci. Semicond. Process.* 39 (2015).
- [23] P.P. Lei, P. Zhang, Q.H. Yuan, Z. Wang, L.L. Dong, S.Y. Song, X. Xu, X.L. Liu, J. Feng, H.J. Zhang, Yb<sup>3+</sup>/Er<sup>3+</sup>-Codoped Bi<sub>2</sub>O<sub>3</sub> nanospheres: probe for upconversion luminescence imaging and binary contrast agent for computed tomography imaging, *ACS Appl. Mater. Interfaces* 7 (2015).
- [24] P.S. Yu, L.B. Su, W. Guo, J. Xu, Photoluminescence and energy transfer progress in Er-doped Bi<sub>2</sub>O<sub>3</sub>-GeO<sub>2</sub> glasses, *J. Lumin.* 187 (2017).
- [25] J. Divya, N.J. Shivaramu, W. Purcell, W.D. Roos, H.C. Swart, Multifunction applications of Bi<sub>2</sub>O<sub>3</sub>:Eu<sup>3+</sup> nanophosphor for red light emission and photocatalytic activity, *Appl. Surf. Sci.* 497 (2019).
- [26] S. Damodaraiah, V.R. Prasad, Y.C. Ratnakaram, Impact of Bi<sub>2</sub>O<sub>3</sub> on Structural Properties and Lasing Effects in Nd<sup>3+</sup> Doped Bismuth Phosphate Glasses at 1.053 Emission, *Spectrochimica Acta Part a-Molecular and Biomolecular Spectroscopy*, 2017, p. 181.
- [27] Q.X. Zhao, H. Suo, Z.Y. Zhang, G. Zhang, C.F. Guo, Simultaneously controlling phase, morphology and up-conversion luminescence via lanthanide doping in Bi<sub>2</sub>O<sub>3</sub>: Yb<sup>3+</sup>/Tm<sup>3+</sup> nanoparticles, *Ceram. Int.* 46 (2020).
- [28] P. Siriwong, T. Thongtem, A. Phuruangrat, S. Thongtem, Hydrothermal synthesis, characterization, and optical properties of wolframite ZnWO<sub>4</sub> nanorods, *CrystEngComm* 13 (2010).
- [29] X.M. Sun, J. Wu, Q.F. Li, Q.Z. Liu, Y.F. Qi, L. You, Z. Ji, P. He, P.F. Sheng, J.X. Ren, W.B. Zhang, J. Lu, J. Zhang, Fabrication of BiOIO<sub>3</sub> with induced oxygen vacancies for efficient separation of the electron-hole pairs, *Appl. Catal. B Environ.* 218 (2017).
- [30] M. Zhou, J. Wu, H.N. Wang, D.Y. Guan, X.F. Dong, J.M. Wang, T. Jia, Q.Z. Liu, Fabrication of Z-Scheme Heterojunction G-C<sub>3</sub>N<sub>4</sub>/Yb<sup>3+</sup>-Bi<sub>2</sub>O<sub>3</sub> Photocatalysts with Enhanced Photocatalytic Performance under Visible Irradiation for Hg0 Removal, vol. 34, *Energy & Fuels*, 2020.
- [31] J. Wu, K. Xu, Q.Z. Liu, Z. Ji, C.H. Qu, XuemeiQi, H. Zhang, Y. Guan, P. He, L.J. Zhu, Controlling Dominantly Reactive (010) Facets and Impurity Level by In-Situ Reduction of BiOIO<sub>3</sub> for Enhancing Photocatalytic Activity, *Applied Catalysis B-Environmental*, 2018, p. 232.
- [32] T. Jia, J. Wu, Z.H. Ji, C. Peng, Q.Z. Liu, M. Shi, J. Zhu, H.N. Wang, D.J. Liu, M. Zhou, Surface Defect Engineering of Fe-Doped Bi<sub>2</sub>O<sub>3</sub> Microflowers for Ameliorating Charge-Carrier Separation and Molecular Oxygen Activation, *Applied Catalysis B-Environmental*, 2021, p. 284.
- [33] J. Yang, D.P. Zheng, X. Xiao, X.J. Wu, X.X. Zuo, J.M. Nan, Iodine self-doping and oxygen vacancies doubly surface-modified BiOIO<sub>3</sub>: facile in situ synthesis, band gap modulation, and excellent visible-light photocatalytic activity, *Chem. Eng. J.* 373 (2019).
- [34] T. Jia, K. Xu, J. Wu, Q.Z. Liu, Y.Y. Lin, M.Y. Gu, F.G. Tian, W.G. Pan, J.X. Wu, Y. Xiao, Constructing 2D BiOIO<sub>3</sub>/MoS<sub>2</sub> Z-scheme heterojunction wrapped by C500

- as charge carriers transfer channel: enhanced photocatalytic activity on gas-phase heavy metal oxidation, *J. Colloid Interface Sci.* (2020) 562.
- [35] H.Q. Cheng, J. Wu, F.G. Tian, Q.Z. Liu, X.M. Qi, Q.W. Li, W.G. Pan, Z.Z. Li, J. Wei, Visible-light photocatalytic oxidation of gas-phase  $Hg^{II}$  by colored  $TiO_2$  nanoparticle-sensitized  $Bi_5O_7I$  nanorods: enhanced interfacial charge transfer based on heterojunction, *Chem. Eng. J.* (2019) 360.
- [36] A.S. Negreira, J. Wilcox, DFT study of Hg oxidation across vanadia-titania SCR catalyst under flue gas conditions, *J. Phys. Chem. C* (2013) 117.
- [37] T. Jia, J. Wu, J. Song, Q.Z. Liu, J.M. Wang, Y.F. Qi, P. He, X.M. Qi, L.T. Yang, P. C. Zhao, In situ self-growing 3D hierarchical  $BiOBr/BiOIO_3$  Z-scheme heterojunction with rich oxygen vacancies and iodine ions as carriers transfer dual-channels for enhanced photocatalytic activity, *Chem. Eng. J.* (2020) 396.
- [38] Y.L. Zhang, Y.C. Zhao, Z. Xiong, T. Gao, B.G. Gong, P.F. Liu, J. Liu, J.Y. Zhang, Elemental Mercury Removal by I-Doped  $Bi_2WO_6$  with Remarkable Visible-Light-Driven Photocatalytic Oxidation, *Applied Catalysis B-Environmental*, 2021, p. 282.
- [39] H.W. Huang, Y. He, R. He, X.X. Jiang, Z.S. Lin, Y.H. Zhang, S.C. Wang, Novel Bi-based iodate photocatalysts with high photocatalytic activity, *Inorg. Chem. Commun.* 40 (2014).
- [40] W.J. Wang, B.B. Huang, X.C. Ma, Z.Y. Wang, X.Y. Qin, X.Y. Zhang, Y. Dai, M. H. Whangbo, Efficient separation of photogenerated electron-hole pairs by the combination of a heterolayered structure and internal polar field in pyroelectric  $BiOIO_3$  nanoplates, *Chem.-Eur. J.* 19 (2013).
- [41] W.L. Huang, Electronic structures and optical properties of  $BiOX$  ( $X = F, Cl, Br, I$ ) via DFT calculations, *J. Comput. Chem.* 30 (2009).
- [42] J.Q. Guo, X. Liao, M.H. Lee, G. Hyett, C.C. Huang, D.W. Hewak, S. Mailis, W. Zhou, Z. Jiang, Experimental and DFT Insights of the Zn-Doping Effects on the Visible-Light Photocatalytic Water Splitting and Dye Decomposition over Zn-Doped  $BiOBr$  Photocatalysts, *Applied Catalysis B-Environmental*, 2019, p. 243.
- [43] G. Di Liberto, S. Tosoni, G. Pacchioni, Nature and role of surface junctions in  $BiOIO_3$  photocatalysts, *Adv. Funct. Mater.* (2021) 31.
- [44] Q. Chen, H.M. Long, M.J. Chen, Y.F. Rao, X.W. Li, Y. Huang, In Situ Construction of Biocompatible Z-Scheme Alpha- $Bi_2O_3/CuBi_2O_4$  Heterojunction for NO Removal under Visible Light, *Applied Catalysis B-Environmental*, 2020, p. 272.
- [45] S.P. Tian, I.A. Bello, J.H. Peng, H.P. Ren, Q. Ma, M. Zhu, K.X. Li, H.Y. Wang, J. Wu, G.Q. Zhu, Fabricating  $Mn_3O_4/\beta-Bi_2O_3$  heterojunction microspheres with enhanced photocatalytic activity for organic pollutants degradation and NO removal, *J. Alloys Compd.* (2021) 854.
- [46] J.W. Fu, Q.L. Xu, J.X. Low, C.J. Jiang, J.G. Yu, Ultrathin 2D/2D  $WO_3/g-C_3N_4$  Step-Scheme H-2-Production Photocatalyst, *Applied Catalysis B-Environmental*, 2019, p. 243.
- [47] S.Q. Wei, F. Wang, P. Yan, M. Dan, W.L. Cen, S. Yu, Y. Zhou, Interfacial coupling promoting hydrogen sulfide splitting on the staggered type II  $g-C_3N_4/r-TiO_2$  heterojunction, *J. Catal.* 377 (2019).
- [48] Q.L. Xu, L.Y. Zhang, J.G. Yu, S. Wageh, A.A. Al-Ghamdi, M. Jaroniec, Direct Z-scheme photocatalysts: principles, synthesis, and applications, *Mater. Today* 21 (2018).
- [49] Q. Wang, K. Domen, Particulate photocatalysts for light-driven water splitting: mechanisms, challenges, and design strategies, *Chem. Rev.* 120 (2020).